

# Image of the time-dependent black hole

Yu Liang<sup>a</sup>, Sen Guo<sup>b</sup>, Kai Lin<sup>c</sup>, Yu-Hao Cui<sup>d</sup>, Yu-Xiang Huang<sup>e</sup>, Tao Yu<sup>a</sup>

<sup>a</sup>China University of Geosciences, Wuhan, 430074, China

<sup>b</sup>Chongqing Normal University, Chongqing, 401331, China

<sup>c</sup>Universidade Federal de Campina Grande, Campina Grande, PB, Brasil

<sup>d</sup>Xiamen University, Xiamen, 361005, China

<sup>e</sup>Guangxi University, Nanning, 530004, China

---

## Abstract

The Event Horizon Telescope's 2024 observations report a shift in the position angle of the brightness asymmetry in M87\*, revealing time variability in the black hole's image. In this analysis, we investigate the time-dependent of a Vaidya black hole. By introducing a mass function that increases linearly with time, along with a conformal transformation, we derive the conformal Vaidya metric and define a new time coordinate  $t_c$ . Using the semi-analytical approach, we analyze the ray trajectories and radiation flux of the Vaidya black hole in the background of a thin accretion disk. We discuss how the observed flux in the Vaidya spacetime evolves as a function of the new time coordinate  $t_c$ . The results show that the facula on the observable plane undergoes radial displacement as  $t_c$  increases, revealing the time-dependent evolution of black hole images.

**Keywords:** Vaidya black hole, Black hole image

---

## 1. Introduction

In 2024, the Event Horizon Telescope (EHT) released a new set of images of the M87\* black hole, based on data collected in 2018, and compared them with the 2017 observations. The results indicated that the position angle of the brightness asymmetry shifted from approximately  $180^\circ$  to around  $215^\circ$ , corresponding to a counterclockwise rotation of about  $35^\circ$  (Akiyama et al., 2024). This dynamic change in angular position has drawn attention to the time-dependent evolution of black hole images. Focusing solely on the spacetime near the black hole and neglecting external effects during light propagation, two potential mechanisms may contribute to the time evolution of black hole images. One possibility is the anisotropy and motion of the surrounding radiation sources, while the other involves the evolution of the spacetime background driven by changes in the black hole's mass. The first hypothesis can be further refined by considering the origin and structure of the emission sources, such as hotspots, dynamic accretion disk models, and so on (Huang et al., 2024; Lee and Gammie, 2021). Previously, Mishra et al. derived the evolution equation for the photon sphere in dynamical black hole spacetimes and investigated its behavior in various black hole models through numerical solutions (Mishra et al., 2019). Solanki and Perlick investigated the dynamical evolution of both the photon sphere and black hole shadow in the context of the Vaidya metric, while Tan analyzed the evolution of black hole shadows in a Kerr-Vaidya-like spacetime (Solanki and Perlick, 2022; Tan, 2023).

The EHT has successively released images of the black holes

at the centers of the M87 galaxy and the Milky Way, providing observational confirmation of the black hole shadows (Akiyama et al., 2019, 2022). These observations have sparked widespread interest among researchers in the optical appearance of black holes. In 1979, Luminet first presented the optical appearance of a Schwarzschild black hole using a semi-analytical method (Luminet, 1979). Since then, numerous studies on black hole shadows have emerged. In 2019, Gralla et al. classified light rays into direct, lensed, and photon ring components by defining the number of orbits, focusing on Schwarzschild and Kerr black holes surrounded by optically and geometrically thin disks (Gralla et al., 2019; Gralla and Lupsasca, 2020). Additionally, Gylchev et al. studied the optical appearance and radiation properties of thin accretion disks around the static Janis–Newman–Winicour naked singularity, while Gan et al. explored the visual appearance of a class of hairy black holes (Gylchev et al., 2019; Gan et al., 2021). In 2022, Perlick and Tsupko conducted a comprehensive review of the current state of research on black hole shadows (Perlick and Tsupko, 2022). In recent years, similar research has also appeared in the works of Peng et al. and other researchers (Peng et al., 2021a,b; Hou et al., 2022; Zeng et al., 2022, 2023; Wang et al., 2023; Huang et al., 2023; Meng et al., 2023, 2024; Cui et al., 2024; Guo et al., 2023, 2024). The approaches adopted in these studies have significantly contributed to the smooth advancement of this research.

However, these studies did not further investigate photon trajectories and radiation flux within a dynamical spacetime background, which constitutes the core focus of this work. In this work, we model the black hole as a Vaidya solution with a linearly increasing mass function and derive its evolving image when surrounded by an accretion disk, thereby providing a the-

---

Email addresses: washy2718@outlook.com (Yu Liang),  
sguophys@126.com (Sen Guo), 1k314159@hotmail.com (Kai Lin)

oretical framework for understanding the observational signatures of temporal variability. The structure of this paper is as follows: we perform a conformal transformation of the Vaidya metric and solve the null geodesic equations in the conformal Vaidya spacetime in Section 2. Section 3 discusses the observer's plane in the conformal Vaidya spacetime and uses ray-tracing to calculate both the direct and secondary images. Section 4 evaluates the observed flux of a black hole surrounded by a thin accretion disk within the conformal spacetime. Finally, we explore the temporal behavior of the observed flux for the Vaidya black hole in the  $t_c - r$  coordinate system and summarize the main findings.

## 2. Null Geodesics of the Vaidya black hole

For a Vaidya black hole with a mass increasing over time, the metric in the ingoing Eddington–Finkelstein coordinate system is given by the following form

$$ds^2 = -fdv^2 + 2dvdr + r^2 d\theta^2 + r^2 \sin^2 \theta d\phi^2 \quad (1)$$

where  $f = 1 - 2m(v)/r$ . In the special case where the mass function  $m(v)$  increases linearly with  $v$ , the metric in Eq. (1) admits an additional conformal Killing vector (Ojako et al., 2020; Solanki and Perlick, 2022). Let  $m(v) = \mu v$ , where  $\mu$  is a positive constant. Then we have

$$f = 1 - \frac{2\mu v}{r} \quad (2)$$

To make the conformal Killing vector explicit, we define the conformal transformation factor as follows

$$\Theta = e^{v_c/r_0} \quad (3)$$

where  $r_0$  is a positive constant. We then perform the following conformal transformation (Solanki and Perlick, 2022)

$$v = r_0\Theta, \quad r = R\Theta. \quad (4)$$

After simplification, the metric in the conformal ingoing Eddington–Finkelstein coordinate system takes the following form

$$ds^2 = \Theta^2 \left( -f_c dv_c^2 + 2dv_c dR + R^2 d\theta^2 + R^2 \sin^2 \theta d\phi^2 \right) \quad (5)$$

where

$$f_c = 1 - \frac{2\mu r_0}{R} - \frac{2R}{r_0} \quad (6)$$

It can be seen that  $\partial/\partial v_c$  is defined as a conformal Killing vector. Moreover, since the metric is conformal to a static spacetime, it can be taken to generate a rotating solution via the Newman–Janis algorithm. At this point, it is necessary to introduce a new time coordinate  $t_c$ , defined as follows

$$v_c = t_c + F_c(R), \quad F_c(R) \equiv \int \frac{dR}{f_c}. \quad (7)$$

After simplification and coordinate transformation, the Vaidya metric in the conformal spherical coordinate system takes the following form

$$ds^2 = \Theta^2 \left( -f_c dt_c^2 + \frac{dR^2}{f_c} + R^2 d\theta^2 + R^2 \sin^2 \theta d\phi^2 \right) \quad (8)$$

To ensure that the conformal spacetime remains timelike, we require  $f_c > 0$ , which implies that the conformal Killing horizon is located at

$$R_{\pm} = \frac{r_0}{4} (1 \pm \sqrt{1 - 16\mu}), \quad \mu < 1/16. \quad (9)$$

where  $R_+$  and  $R_-$  denote the outer and inner conformal Killing horizons, respectively. Accordingly, we have  $-\infty < t_c < +\infty$  and  $R_- < R < R_+$ .

To simplify the analysis, we restrict our attention to null geodesics confined to the equatorial plane. Based on the metric (8), the corresponding Lagrangian is given by

$$\tilde{L} = \frac{\Theta^2}{2} \left[ -f_c \dot{t}_c^2 + \frac{\dot{R}^2}{f_c} + R^2 \dot{\phi}^2 \right] = 0 \quad (10)$$

Since  $\partial/\partial t_c$  is also a conformal Killing vector, both the photon energy  $E$  and angular momentum  $L$  are conserved (Solanki and Perlick, 2022). These conserved quantities are given by

$$\frac{\partial \tilde{L}}{\partial \dot{t}_c} = -\Theta^2 f_c \dot{t}_c \equiv E \quad (11)$$

$$\frac{\partial \tilde{L}}{\partial \dot{\phi}} = \Theta^2 R^2 \dot{\phi} \equiv L \quad (12)$$

When  $\dot{\phi} \neq 0$ , the above three equations lead to the null geodesic equation in the conformal Vaidya spacetime, given by

$$\left[ \frac{1}{R^2} \left( \frac{dR}{d\phi} \right)^2 + \frac{f_c}{R^2} \right] = \frac{1}{b^2} \quad (13)$$

where  $b = L/E$  is the impact parameter. It follows that the photon trajectory in the conformal coordinate system is independent of the time coordinate  $t_c$ .

For light rays that are not captured by a black hole, there exists a periastron  $R_m$  along the trajectory such that  $dR_m/d\phi = 0$ . From Eq. (13), the relationship between the impact parameter and the periastron is given by

$$b = \frac{R_m}{\sqrt{f_c}} = \sqrt{\frac{R_m^3}{R_m - 2\mu r_0 - 2R_m^2/r_0}} \quad (14)$$

Since the radius of the photon sphere  $R_p$  corresponds to the minimum among all periastra, it must also satisfy the condition  $d^2 R/d\phi^2 = 0$ . Solving this condition yields (Solanki and Perlick, 2022)

$$R_p = \frac{r_0}{2} (1 - \sqrt{1 - 12\mu}) \quad (15)$$

By substituting  $R_p$  into Eq. (14), the critical impact parameter  $b_p$  can be determined. When  $b > b_p$ , light rays are deflected but not captured by the black hole, whereas for  $b < b_p$ , they are captured.

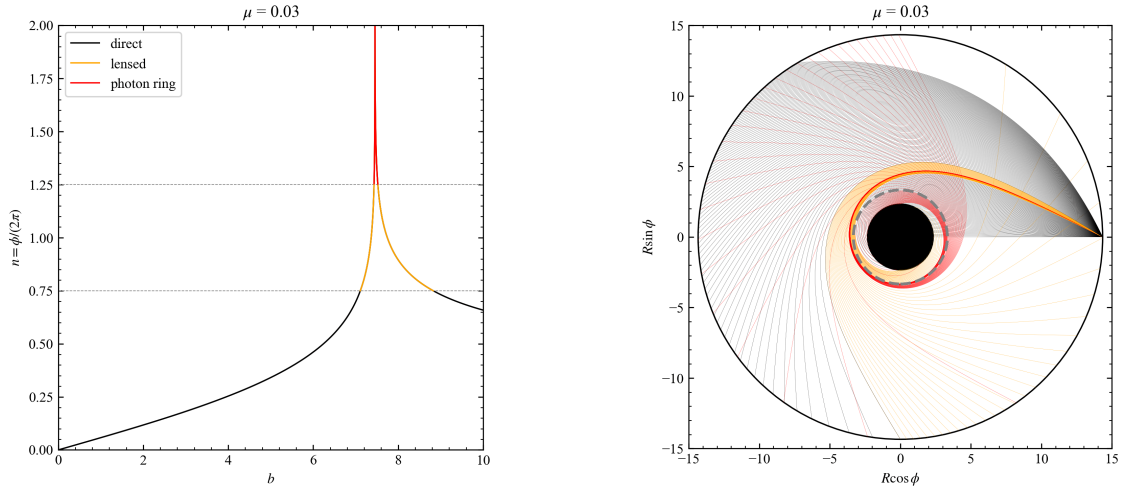


Figure 1: Behavior of photons in the conformal Vaidya spacetime as a function of impact parameter  $b$ . The left panel illustrates the dependence of the orbital number  $n$  is illustrated, with direct, lensed, and photon ring components marked in black, orange, and red, respectively. The right panel shows the corresponding photon trajectories.

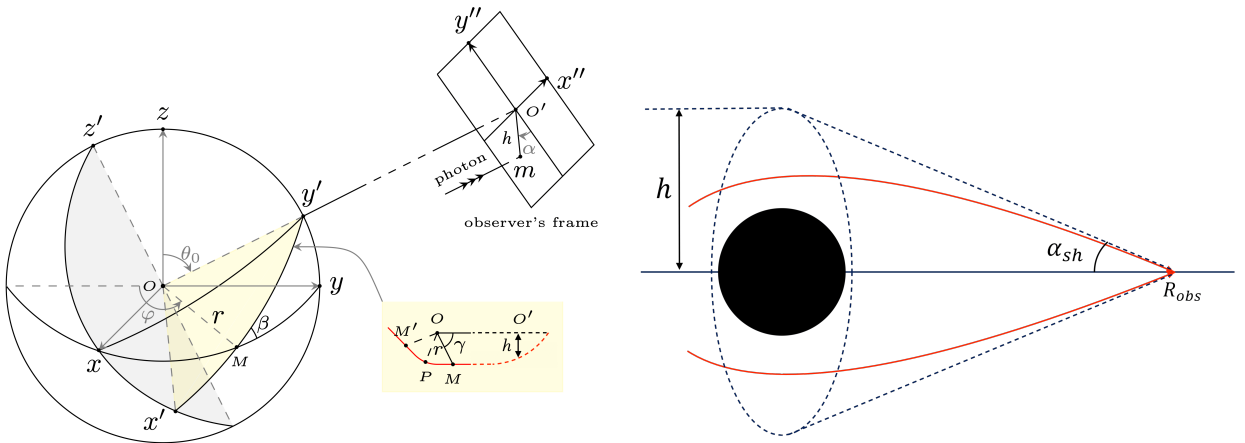


Figure 2: The conformal coordinate system. The left panel follows the coordinate framework introduced by Luminet and Tian (Luminet, 1979; Tian and Zhu, 2019), with two key modifications: (1) the projection distance on the observer's plane is denoted by  $h$  instead of the impact parameter  $b$ ; (2) light rays are assumed to converge at  $R_+$  on the yellow plane. The right panel illustrates the geometric relation among the observer's position  $R_{obs}$ , the angular radius  $\alpha_{sh}$ , and the projection distance  $h$ .

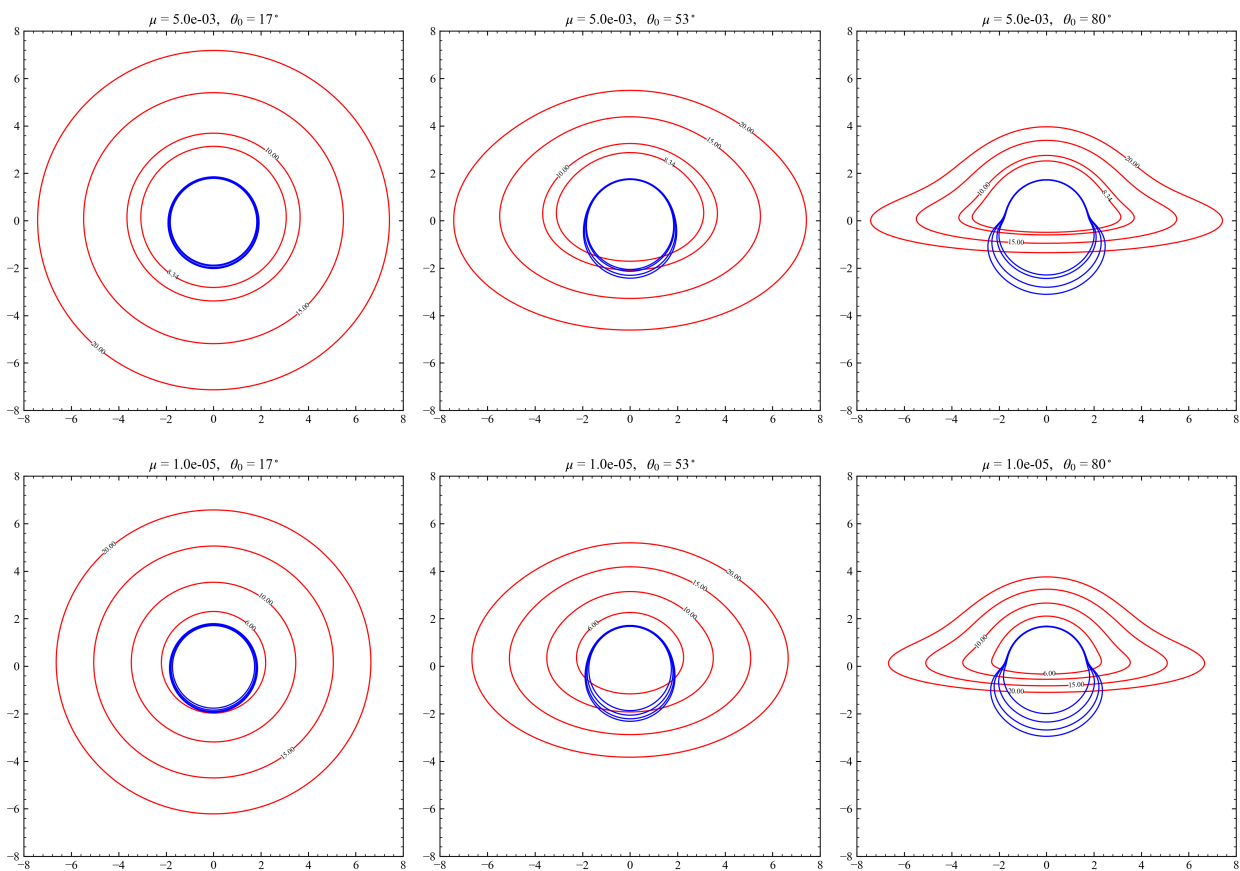


Figure 3: The direct (red) and secondary (blue) images of a thin accretion disk in the conformal Vaidya spacetime background.

### 3. Ray trajectory of the Vaidya black hole

#### 3.1. The deflection angle of the light ray

For a Schwarzschild black hole, light rays are typically assumed to originate from or propagate to spatial infinity. In contrast, for the conformal Vaidya black hole, the radial coordinate  $R$  is bounded between  $R_-$  and  $R_+$ , implying that light rays must be considered as originating from or terminating at  $R_+$ . By defining  $R = 1/U$ , Eq. (13) can be recast as

$$\left(\frac{dU}{d\phi}\right)^2 = 2M_0U^3 - U^2 + \frac{2U}{r_0} + \frac{1}{b^2} \equiv G(U) \quad (16)$$

where  $M_0 \equiv \mu r_0$  is a constant. Throughout this paper, we set  $M_0 = 1$  for all calculations.

Although the above expression gives the differential form of  $\phi$ , its integral form is required to accurately compute the deflection angle. For a light ray emitted from  $R_+$ , if  $b < b_p$ , or if  $b > b_p$  but the ray does not reach the periastron  $R_m$ , the deflection angle is given by the following integral expression

$$\phi = \int_{U_+}^U \frac{dU}{\sqrt{G(U)}} \quad (17)$$

If  $b > b_p$  and the photon has already passed through the periastron  $R_m$ , then the deflection angle is given by

$$\phi = 2 \int_{U_+}^{U_m} \frac{dU}{\sqrt{G(U)}} - \int_{U_+}^U \frac{dU}{\sqrt{G(U)}} \quad (18)$$

where  $U_+ = 1/R_+$  and  $U_m = 1/R_m$ .

We define the orbit number as  $n \equiv \phi/2\pi$ , where  $\phi$  is the total azimuthal change outside the horizon. When  $n < 3/4$ , the photon crosses the equatorial plane only once; when  $n > 3/4$ , it crosses at least twice; and when  $n > 5/4$ , it crosses at least three times (Gralla et al., 2019). The relationship between the orbit number  $n$  and the impact parameter  $b$ , as well as the corresponding light trajectories, is shown in Fig. 1 for  $\mu = 0.03$ . As illustrated, the photon trajectories no longer extend to spatial infinity but instead converge at  $R_+$ . According to Eq. (9),  $R_+$  increases as  $\mu$  decreases. In the limit  $\mu \rightarrow 0$ ,  $R_+ \rightarrow +\infty$ , and the photon trajectories approach those of a Schwarzschild black hole (Tan, 2023).

#### 3.2. Ray trajectory

We consider a Vaidya black hole surrounded by a geometrically thin accretion disk. Assume that the observer's image plane is positioned at  $R_{obs}$  and inclined at an angle  $\theta_0$  relative to the equatorial plane. A conformal coordinate system is introduced, as illustrated in Fig. 2. The construction of Fig. 2 follows the framework established by Luminet and Tian (Luminet, 1979; Tian and Zhu, 2019), with two key modifications. First, the distance on the observer's plane is described by a new parameter  $h$ , which is determined by the observer's position and the angular radius, rather than by the impact parameter  $b$ . Second, the light rays are assumed to converge at  $R_+$ . Despite these changes, the original angular relationships remain valid and continue to satisfy the following expressions

$$\cos \gamma = \frac{\cos \alpha}{\sqrt{\cos^2 \alpha + \cot^2 \theta_0}} \quad (19)$$

When specifying the position of the observation plane, it is important to note that  $R_{obs}$  must lie strictly between the two horizons and cannot coincide with either horizon. Based on the geometric relationships depicted in Fig. 2, we obtain

$$h = R_{obs} \tan \alpha_{sh} \quad (20)$$

where  $\alpha_{sh}$  is the angular radius. For a light ray with impact parameter  $b$ , the corresponding angular radius  $\alpha_{sh}$  satisfies the following relation (Solanki and Perlick, 2022)

$$\tan \alpha_{sh} = \sqrt{\frac{f_c(R_{obs})}{R_{obs}^2/b^2 - f_c(R_{obs})}} \quad (21)$$

For a light source located at  $R$ , the deflection angle  $\phi = \gamma$  for the direct image can be computed using Eq. (17) or Eq. (18). For the  $(1+n)$ th-order image, the deflection angle is given by  $\phi = 2n\pi - \gamma$ , and can be evaluated using Eq. (18). In practice, by substituting known parameters  $(\phi, R)$  and reformulating the equation as a root-finding problem, the unknown impact parameter  $b$  can be efficiently determined using Python or other numerical solvers.

To determine the inner edge of the accretion disk, it is necessary to compute the innermost stable circular orbit (ISCO). For the spacetime described by the metric in Eq. (8), the conditions for a circular orbit are  $\dot{r} = 0$  and  $\ddot{r} = 0$ . Imposing these conditions yields

$$E^2 = \frac{2\Theta^2 (f_c^2 + R/r_0 f_c)}{2f_c - Rf_c'}, \quad (22)$$

$$L^2 = \frac{\Theta^2 R^3 (f_c' + 2/r_0)}{2f_c - Rf_c'}. \quad (23)$$

Given the Hamiltonian of the test particle  $\tilde{H} = -1/2$ , the corresponding effective potential is expressed as

$$V_m(R) = f_c \left( \frac{L^2}{R^2} + \Theta^2 \right) \quad (24)$$

By combining the equation  $V''(R) = 0$  with the three equations above, the ISCO radius is found to satisfy the following equation

$$6R^4 - 8r_0R^3 + (1 + 22\mu)r_0^2R^2 - 8\mu r_0^3R + 12\mu^2r_0^4 = 0 \quad (25)$$

An analysis of Eq. (25) reveals that for  $\mu < 6.063 \times 10^{-3}$ , there exist four real roots, with the ISCO corresponds to the second smallest among them. For  $\mu > 6.063 \times 10^{-3}$ , no ISCO exists within the physically admissible region. Moreover, the ISCO radius increases monotonically with  $\mu$ , attaining its minimum value of 6 at  $\mu = 0$ , and reaching a maximum of approximately  $R_{ISCO} \approx 9.421$  as  $\mu$  approaches  $6.063 \times 10^{-3}$ .

Figure 3 displays the direct (red) and secondary (blue) images of a thin accretion disk in the conformal Vaidya spacetime for  $\mu = 5 \times 10^{-3}$  and  $10^{-5}$ . In both cases, the observer is located at a radial position of  $0.9R_+$ . As shown in the figure, for a fixed value of  $\mu$ , both the direct and secondary images are distorted as the inclination angle varies. Conversely, for a fixed inclination angle, the image size decreases with decreasing  $\mu$ .

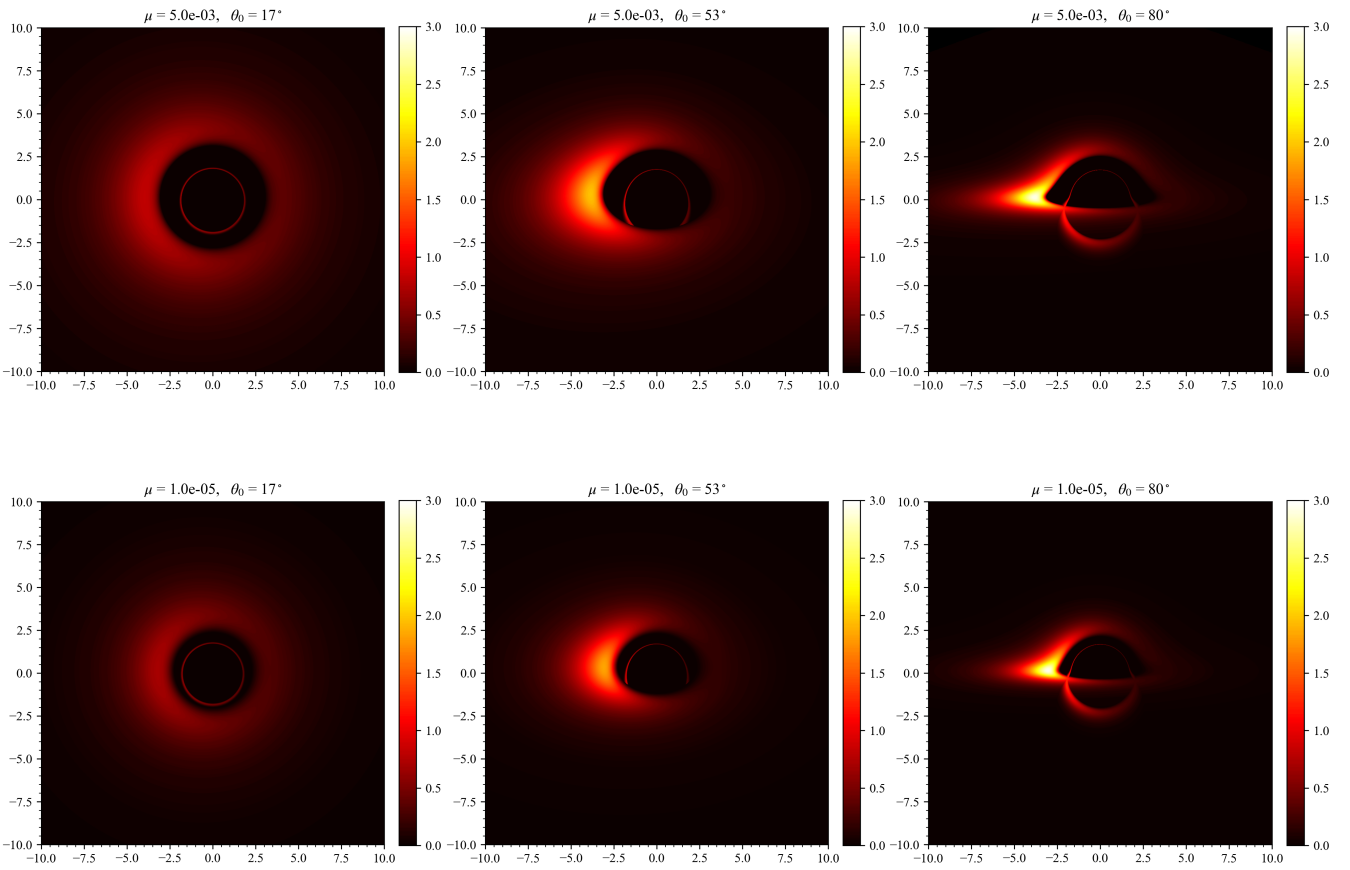


Figure 4: The observed flux from the conformal Vaidya black hole, surrounded by thin accretion disk.

#### 4. Radiation flux of the vaidya black hole

Previous studies have derived expressions for the radiative flux in thin accretion disk models, where the self-gravity of disk is neglected and the background spacetime is assumed to be stationary and asymptotically flat (Novikov and Thorne, 1973; Page and Thorne, 1974). As shown earlier, the metric (8) is conformal to a static spacetime, and it can be readily verified that it becomes asymptotically flat at  $R_+$ . Therefore, the radiative flux in the conformal Vaidya background is given by the following expression

$$I = -\frac{\dot{M}_0}{4\pi\sqrt{-g}}\frac{\Omega_{,R}}{(E-\Omega L)^2}\int_{R_{in}}^R(E-\Omega L)L_{,R}dR \quad (26)$$

where  $\dot{M}_0$  is the mass accretion rate,  $g$  is the metric determinant, and  $R_{in}$  is the inner boundary of the accretion disk, usually ISCO.  $E$ ,  $L$ , and  $\Omega$  represent the energy, angular momentum, and angular velocity, and are given by

$$E = -\frac{g_{tt}}{\sqrt{-g_{tt} - g_{\phi\phi}\Omega^2}} \quad (27)$$

$$L = \frac{g_{\phi\phi}\Omega}{\sqrt{-g_{tt} - g_{\phi\phi}\Omega^2}} \quad (28)$$

$$\Omega = \frac{d\phi}{dt} = \sqrt{-\frac{g_{t\phi,R}}{g_{\phi\phi,R}}} \quad (29)$$

For a thin accretion disk confined to the equatorial plane, the corresponding components are given by

$$g_{tt} = -\Theta^2 f_c, \quad g_{\phi\phi} = \Theta^2 R^2, \quad g = -\Theta^8 R^4. \quad (30)$$

By combining the above equations and rearranging Eq. (26) to isolate the time variable  $t_c$ , we obtain

$$I(t_c, R) = I(0, R)e^{-4t_c} \equiv I_0(R)e^{-4t_c} \quad (31)$$

where  $I_0(R)$  is the radiation flux at  $t_c = 0$ .

Owing to the gravitational field of the black hole, the observed flux experiences varying degrees of gravitational redshift. According to Ref. (Luminet, 1979), the observed flux can be expressed as

$$I_{obs} = \frac{I}{(1+z)^4} \quad (32)$$

where  $(1+z)$  denotes the redshift factor, given by

$$1+z = \frac{1+b\Omega\sin\theta_0\sin\alpha}{\sqrt{-g_{tt} - g_{\phi\phi}\Omega^2}} \quad (33)$$

Similarly, let the redshift factor be  $1+z_0$  at  $t_c = 0$ , then we obtain

$$1+z = (1+z_0)e^{-t_c} \quad (34)$$

By combining Eqs. (31), (32), and (34), we find that the observed flux is independent of the time coordinate  $t_c$ , and can be expressed as

$$I_{obs} = \frac{I_0}{(1+z_0)^4} \quad (35)$$

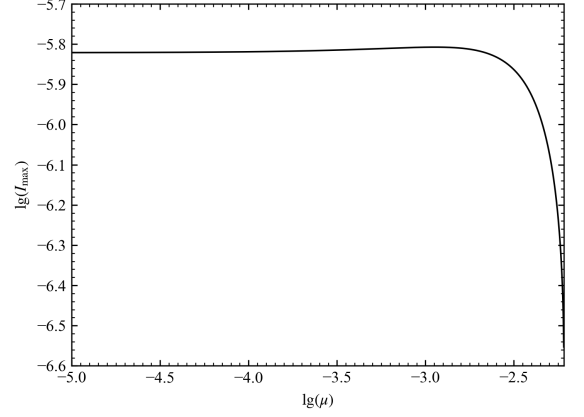


Figure 5: The relationship between the peak radiation flux  $I_{max}$  and the parameter  $\mu$  is illustrated, with both quantities plotted on a logarithmic scale.

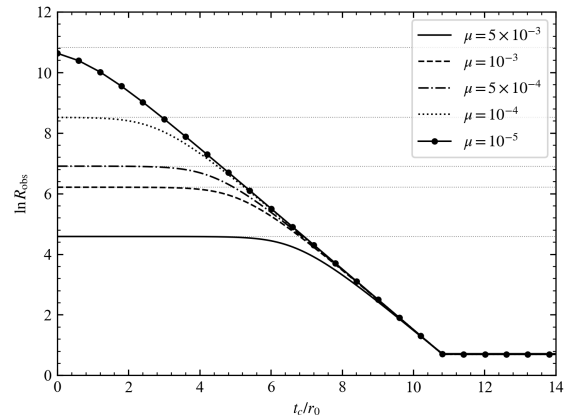


Figure 6: The evolution of  $R_{obs}$  as a function of  $t_c/r_0$  is shown for an observer located at  $r_{obs} = 10^5$ . The solid, dashed, dotted, dash-dotted, and solid-dot curves correspond to  $\mu$  values of  $5 \times 10^{-3}$ ,  $10^{-3}$ ,  $5 \times 10^{-4}$ ,  $10^{-4}$ , and  $10^{-5}$ , respectively. The gray dotted line represents the conformal Killing horizon  $R_+$  associated with each value of  $\mu$ .

Figure 4 displays the observed flux from thin accretion disk in a conformal Vaidya spacetime for  $\mu = 5 \times 10^{-3}$  and  $10^{-5}$ . The maximum flux value  $I_{max}$  is excluded in each panel, and the flux at each grid point corresponds to the sum of the direct and secondary observed fluxes. For both values of  $\mu$ , the distance between the observation plane and the black hole center is uniformly set to  $0.9R_+$ . It can be seen that variations in  $\mu$  have a relatively small effect on the magnitude of the relative observed flux. Figure 5 depicts the variation of the maximum observed flux  $I_{max}$  as a function of  $\mu$ . As shown in the figure,  $I_{max}$  initially increases slightly and then decreases rapidly as  $\mu$  increases.

#### 5. Results

By applying the conformal transformation given in Eq. (4), the coordinate system can be mapped from  $(t_c, R, \theta, \phi)$  to  $(t_c, r, \theta, \phi)$ , enabling a more physically intuitive visualization of the Vaidya black hole image. This transformation also facilitates further investigation into how the image evolves with respect to the time parameter  $t_c$ . Although the time parameter  $t_c$  is

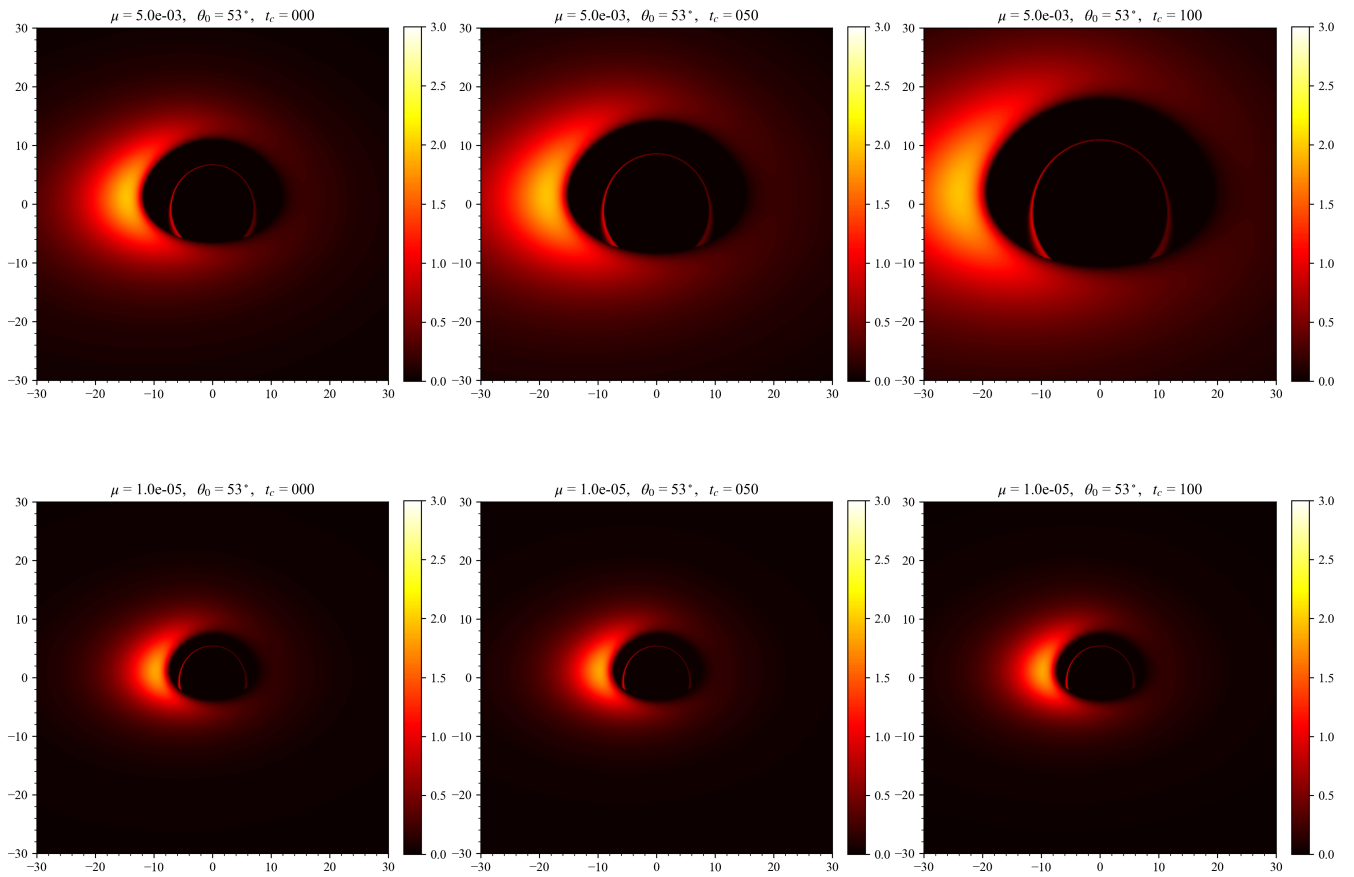


Figure 7: The observed flux of the Vaidya black hole evolves with the time coordinate  $t_c$  for different values of  $\mu$ .

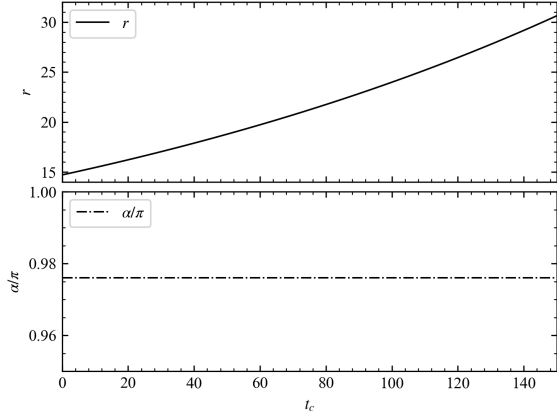


Figure 8: The evolution of the observed flux peak position as a function of  $t_c$  for  $\mu = 5 \times 10^{-3}$ . The upper panel shows the radial evolution, while the lower panel illustrates the angular variation. It is observed that the radial distance increases with  $t_c$ , whereas the angular position remains nearly constant.

not be equivalent to the physical time  $t$ , the results still provide valuable insights into the appearance of a Vaidya black hole in physical spacetime.

Since the coordinate transformation only modifies the radial component, all angular quantities remain unchanged, although their association shifts from  $R$  to  $r$ ; the same applies to the radiation flux. Moreover, the observer's position is fixed in the  $(t_c, r, \theta, \phi)$  coordinate system, implying that  $r_{obs}$  remains constant, while the corresponding location  $R_{obs}$  in the conformal coordinates evolves dynamically with  $t_c$ .

Figure 6 illustrates the evolution of  $R_{obs}$  as a function of  $t_c/r_0$  for various values of  $\mu$ , with the observer fixed at  $r_{obs} = 10^5$ . It is evident from Fig. 6 that as  $t_c$  increases, the increase in black hole mass is equivalent to the observer gradually approaching the black hole in the conformal coordinate system. Eventually, the observer at fixed  $r_{obs}$  asymptotically approaches  $R_-$  in the conformal frame. For small values of  $\mu$ , this corresponding time interval can be approximated as

$$\Delta t_c \approx r_0 \ln \frac{r_{obs}}{R_-} \quad (36)$$

Moreover, the projected distance  $h_r$  on the observer's plane in the  $(t_c, r, \theta, \phi)$  coordinate system can be derived from Eqs. (20) and (4) as follows

$$h_r = r_{obs} \tan \alpha_{sh} = h_c \Theta(t_c, R_{obs}) \quad (37)$$

With these preparations in place, the image of the Vaidya black hole can now be constructed in the  $(t_c, r, \theta, \phi)$  coordinate system.

Figure 7 presents the observed flux at different values of  $t_c$  for  $\mu = 5 \times 10^{-3}$  and  $10^{-5}$ . As shown in Fig. 7, for  $\mu = 5 \times 10^{-3}$ , the shadow size increases significantly with increasing  $t_c$ , and the peak flux position shifts outward in the radial direction. In contrast, for  $\mu = 10^{-5}$ , the image shows much weaker temporal variations over the same interval. Figure 8 depicts the evolution of the location of the maximum observed flux as a function of  $t_c$  for  $\mu = 5 \times 10^{-3}$ . This further confirms that the peak flux location moves outward in the radial direction with time, while remaining stationary in the angular direction.

## 6. Conclusions and discussion

This paper investigates a time-dependent black hole described by the Vaidya metric, where the mass function  $m(v)$  is assumed to increase linearly. By introducing a conformal factor and a redefined time coordinate as  $t_c$ , we analytically derived and numerically computed the ray trajectories and radiation flux in the conformal coordinate system. We further employed the conformal transformation to explore the time-dependent behavior of the Vaidya black hole in the  $t_c - r$  coordinate system. Our main findings can be summarized as follows:

1. For an observer located at  $r_{obs}$ , the time-dependent increase in black hole mass is equivalent to the observer gradually approaching the black hole in the conformal coordinate system.
2. As  $t_c$  increases, the apparent size of the black hole shadow on the observation plane grows accordingly.
3. The maximum observed flux initially increases slowly and then decreases rapidly as  $\mu$  continues to grow.
4. For a fixed value of  $\mu$ , the facula on the observable plane exhibits a radial shift over time, while its azimuthal position remains unchanged. Since  $\mu$  is typically small, substantial radial displacement may not be observable within a finite observational timescale. However, such displacement may become detectable over a sufficiently long period. The position-angle rotation of brightness asymmetry observed by the EHT may instead be attributed to variations in the emission source.

In future work, we aim to provide a theoretical explanation for and reproduce the counterclockwise rotation of the brightest region observed by the EHT. To this end, we plan to investigate more sophisticated time-dependent black hole metrics and models of radiation source.

## Acknowledgments

This work is supported by the Brazilian agencies Fapesq-PB, Fund Project of Chongqing Normal University (Grant Number: 24XLB033) and the National Natural Science Foundation of China (Grants Number: 42230207, 42074191).

## References

- Akiyama, K., et al. (Event Horizon Telescope), 2019. First M87 Event Horizon Telescope Results. I. The Shadow of the Supermassive Black Hole. *Astrophys. J. Lett.* 875, L1. doi:10.3847/2041-8213/ab0ec7, arXiv:1906.11238.
- Akiyama, K., et al. (Event Horizon Telescope), 2022. First Sagittarius A\* Event Horizon Telescope Results. I. The Shadow of the Supermassive Black Hole in the Center of the Milky Way. *Astrophys. J. Lett.* 930, L12. doi:10.3847/2041-8213/ac6674, arXiv:2311.08680.
- Akiyama, K., et al. (Event Horizon Telescope), 2024. The persistent shadow of the supermassive black hole of M 87. I. Observations, calibration, imaging, and analysis. *Astron. Astrophys.* 681, A79. doi:10.1051/0004-6361/202347932.
- Cui, Y.H., Guo, S., Huang, Y.X., Liang, Y., Lin, K., 2024. Optical appearance of numerical black hole solutions in higher derivative gravity. *Eur. Phys. J. C* 84, 772. doi:10.1140/epjc/s10052-024-13153-2, arXiv:2408.03387.
- Gan, Q., Wang, P., Wu, H., Yang, H., 2021. Photon spheres and spherical accretion image of a hairy black hole. *Phys. Rev. D* 104, 024003. doi:10.1103/PhysRevD.104.024003, arXiv:2104.08703.

- Gralla, S.E., Holz, D.E., Wald, R.M., 2019. Black Hole Shadows, Photon Rings, and Lensing Rings. *Phys. Rev. D* 100, 024018. doi:10.1103/PhysRevD.100.024018, arXiv:1906.00873.
- Gralla, S.E., Lupsasca, A., 2020. Lensing by Kerr Black Holes. *Phys. Rev. D* 101, 044031. doi:10.1103/PhysRevD.101.044031, arXiv:1910.12873.
- Guo, S., Huang, Y.X., Liang, E.W., Liang, Y., Jiang, Q.Q., Lin, K., 2024. Image of the Kerr–Newman Black Hole Surrounded by a Thin Accretion Disk. *Astrophys. J.* 975, 237. doi:10.3847/1538-4357/ad7d85, arXiv:2411.07914.
- Guo, S., Li, G.R., Liang, E.W., 2023. Optical appearance of a thin-shell wormhole with a Hayward profile. *Eur. Phys. J. C* 83, 663. doi:10.1140/epjc/s10052-023-11842-y, arXiv:2210.03010.
- Gyulchev, G., Nedkova, P., Vetsov, T., Yazadjiev, S., 2019. Image of the Janis–Newman–Winicour naked singularity with a thin accretion disk. *Phys. Rev. D* 100, 024055. doi:10.1103/PhysRevD.100.024055, arXiv:1905.05273.
- Hou, Y., Zhang, Z., Yan, H., Guo, M., Chen, B., 2022. Image of a Kerr–Melvin black hole with a thin accretion disk. *Phys. Rev. D* 106, 064058. doi:10.1103/PhysRevD.106.064058, arXiv:2206.13744.
- Huang, J., Zhang, Z., Guo, M., Chen, B., 2024. Images and flares of geodesic hot spots around a Kerr black hole. *Phys. Rev. D* 109, 124062. doi:10.1103/PhysRevD.109.124062, arXiv:2402.16293.
- Huang, Y.X., Guo, S., Cui, Y.H., Jiang, Q.Q., Lin, K., 2023. Influence of accretion disk on the optical appearance of the Kazakov–Solodukhin black hole. *Phys. Rev. D* 107, 123009. doi:10.1103/PhysRevD.107.123009, arXiv:2311.00302.
- Lee, D., Gammie, C.F., 2021. Disks as Inhomogeneous, Anisotropic Gaussian Random Fields. *Astrophys. J.* 906, 39. doi:10.3847/1538-4357/abc8f3, arXiv:2011.07151.
- Luminet, J.P., 1979. Image of a spherical black hole with thin accretion disk. *Astron. Astrophys.* 75, 228–235.
- Meng, Y., Kuang, X.M., Wang, X.J., Wang, B., Wu, J.P., 2023. Images from disk and spherical accretions of hairy Schwarzschild black holes. *Phys. Rev. D* 108, 064013. doi:10.1103/PhysRevD.108.064013, arXiv:2306.10459.
- Meng, Y., Kuang, X.M., Wang, X.J., Wang, B., Wu, J.P., 2024. Images of hairy Reissner–Nordström black hole illuminated by static accretions. *Eur. Phys. J. C* 84, 305. doi:10.1140/epjc/s10052-024-12686-w, arXiv:2401.05634.
- Mishra, A.K., Chakraborty, S., Sarkar, S., 2019. Understanding photon sphere and black hole shadow in dynamically evolving spacetimes. *Phys. Rev. D* 99, 104080. doi:10.1103/PhysRevD.99.104080, arXiv:1903.06376.
- Novikov, I.D., Thorne, K.S., 1973. in: DeWitt, C., DeWitt, B. (Eds.), *Black Holes*. Gordon and Breach, New York.
- Ojako, S., Goswami, R., Maharaj, S.D., Narain, R., 2020. Conformal symmetries in generalised Vaidya spacetimes. *Class. Quant. Grav.* 37, 055005. doi:10.1088/1361-6382/ab5e2d, arXiv:1904.08120.
- Page, D.N., Thorne, K.S., 1974. Disk-Accretion onto a Black Hole. Time-Averaged Structure of Accretion Disk. *Astrophys. J.* 191, 499–506. doi:10.1086/152990.
- Peng, J., Guo, M., Feng, X.H., 2021a. Influence of quantum correction on black hole shadows, photon rings, and lensing rings. *Chin. Phys. C* 45, 085103. doi:10.1088/1674-1137/ac06bb, arXiv:2008.00657.
- Peng, J., Guo, M., Feng, X.H., 2021b. Observational signature and additional photon rings of an asymmetric thin-shell wormhole. *Phys. Rev. D* 104, 124010. doi:10.1103/PhysRevD.104.124010, arXiv:2102.05488.
- Perlick, V., Tsupko, O.Y., 2022. Calculating black hole shadows: Review of analytical studies. *Phys. Rept.* 947, 1–39. doi:10.1016/j.physrep.2021.10.004, arXiv:2105.07101.
- Solanki, J., Perlick, V., 2022. Photon sphere and shadow of a time-dependent black hole described by a Vaidya metric. *Phys. Rev. D* 105, 064056. doi:10.1103/PhysRevD.105.064056, arXiv:2201.03274.
- Tan, H.S., 2023. Shadows of Kerr–Vaidya-like black holes. *Class. Quant. Grav.* 40, 195010. doi:10.1088/1361-6382/acf180, arXiv:2301.04967.
- Tian, S.X., Zhu, Z.H., 2019. Testing the Schwarzschild metric in a strong field region with the Event Horizon Telescope. *Phys. Rev. D* 100, 064011. doi:10.1103/PhysRevD.100.064011, arXiv:1908.11794.
- Wang, X.J., Kuang, X.M., Meng, Y., Wang, B., Wu, J.P., 2023. Rings and images of Horndeski hairy black hole illuminated by various thin accretions. *Phys. Rev. D* 107, 124052. doi:10.1103/PhysRevD.107.124052, arXiv:2304.10015.
- Zeng, X.X., He, K.J., Li, G.P., Liang, E.W., Guo, S., 2022. QED and accretion flow models effect on optical appearance of Euler–Heisenberg black holes. *Eur. Phys. J. C* 82, 764. doi:10.1140/epjc/s10052-022-10733-y, arXiv:2209.05938.
- Zeng, X.X., He, K.J., Pu, J., Li, G.p., Jiang, Q.Q., 2023. Holographic Einstein rings of a Gauss–Bonnet AdS black hole. *Eur. Phys. J. C* 83, 897. doi:10.1140/epjc/s10052-023-12079-5, arXiv:2302.03692.